Residual ferrite in martensitic stainless steels: the effect of mechanical strength contrast on ductility

Alvise Miotti Bettanini[a,*], Florent Hannard[a], Jean-Denis Mithieux[b], Guillaume Badinier[b], Pascal J. Jacques[a], Thomas Pardoen[a], Laurent Delannay[a]

[a] *Institute of Mechanics, Materials and Civil Engineering, Universite catholique de Louvain, B-1348 Louvain-la-Neuve, Belgium*
[b] *Aperam Research Center, BP 15, 62230 Isbergues, France*

Abstract

Ductile damage process of a martensitic stainless steel with 15 vol.% of residual ferrite and two populations of carbide particles is investigated using a combined multiscale experimental and modelling approach. Whereas Nb-rich carbides contribute to grain refinement, coarser Cr-rich carbides are preferential damage nucleation sites. Three different heat treatments are applied to partially dissolve Cr-carbide particles while keeping the same ratio of ferrite versus martensite volume fraction. Surprisingly, ductility decreases with decreasing volume fraction of Cr-carbides. Nanoindentation mapping indicates that the strength contrast between ferrite and martensite increases with carbide dissolution. According to finite element simulations of strain partitioning inside the two phase microstructure, the stress triaxiality in ferrite increases with the mechanical strength contrast. This promotes void nucleation and growth, reducing the fracture strain.

*Corresponding author

1. Introduction

The automotive industry faces increasingly severe constraints on gas emission, weight and safety of car vehicles. Aside from evolution in propelling technology, significant margin of progress is still open regarding the weight reduction of chassis through an increase of strength and toughness of the structural components. Such enhancements should be achieved while minimizing the processing cost and the environmental impact. High strength steels remain a key solution as proven by the progress made over the last decade regarding the mechanical performances of new generations of steels, which gives much hope for future improvements [1], [2], [3]. Among these, Martensitic Stainless Steels (MSS) exhibit excellent combination of mechanical properties and corrosion resistance [4, 5, 6].

MSS are Fe-Cr-C alloys heat-treated in the austenitic temperature range and then quenched to form martensite. This relatively straightforward process produces microstructures with a large fraction of martensite, residual ferrite and secondary precipitation carbides. A key element in the strengthening strategies is the control of the carbide precipitation. Small addition of strong MC-type carbide forming elements like Nb or Ti is beneficial, contributing to both grain refinement and precipitation strengthening [7],[8], [2],[9]. On the other hand, the presence of coarse $M_{23}C_6$ (M=Cr,Fe) carbides is detrimental for corrosion resistance, mechanical properties and weldability. The volume fraction of coarse carbides should hence be minimized by optimizing the heat treatment conditions [10, 11, 12, 13]. In addition, residual ferrite, which is the result of a slow austenization kinetic [14, 15, 16, 17, 18], can reach volume fractions as high as 20 vol.%. This has a significant influence on the final mechanical properties. The structure of MSS with residual ferrite resembles the one of Dual-Phase (DP) steels, about which there is substantial ongoing research [19, 20, 21, 22, 23, 24], which is likely to apply also to MSS. Recent studies on DP steels have for instance unravelled the impact of martensite volume fraction ($V_{\alpha'}$), martensite carbon content ($C_{\alpha'}$) and grain size on the plastic behaviour, see e.g. Delince et al. [25], Pierman et al. [26].

Heterogeneities in the DP steels microstructure generate inhomogeneous distribution of stress and strain during plastic deformation. Recently, Kang et al. [27] mapped the strain partitioning at the grain scale with μ-DIC (Digital Image Correlation). They found that tempering of martensite changes the distribution of strain across the dual-phase microstructure and this, in turn, influences damage accumulation, ductility and tensile strength. Damage depends also on the ratio of martensite and ferrite [28, 29]. Lai et al. [30] characterized damage evolution in DP steels as a function of martensite content. At low $V_{\alpha'}$, interface decohesion between martensite islands and ferrite matrix is the dominant mechanism of damage initiation. On the contrary, if the martensite volume fraction ($V_{\alpha'}$) is increased, martensite cracking is found to be the main origin of damage.

In addition, the presence of coarse carbides can significantly affect damage evolution. These precipitates, which often show low coherency with the surrounding matrix, are favourable sites for damage nucleation in steel [31, 32, 33, 34]. Thus, fracture strain can be increased by changing the particle distribution, i.e. reducing their size and/or volume fraction and increasing the interparticle distance [31], which is the trend followed by all ductile metals [35].

The damage initiation in a ferrite-martensite DP structure was recently modelled by de Geus et al. [36, 37] who found that increasing the mechanical strength contrast significantly promotes damage initiation in DP steel. Phase topology is relevant too: for instance, a small region of ferrite enclosed by islands of hard martensite is a preferential damage initiation site due to local rise of plastic strain and stress triaxiality. Yerra et al. [38] who studied damage nucleation by interface debonding in a duplex ferrite-austenite microstructure found stress triaxiality to be the main parameter controlling the nucleation, growth and coalescence of voids. All the studies cited above are of prime importance for the development of new families of DP steels in which ferrite is almost always the dominant phase. However, much less is known about DP steels with high fraction of martensite ($V_{\alpha'} > 80$ vol.%), which is of practical relevance for the development of low-carbon MSS.

The present paper describes a combined experimental/modelling investiga-

tion of the plastic strain distribution and damage mechanisms occurring in a newly developed Nb-modified MSS for structural automotive applications. The key question motivating this work is the observation of a significant reduction of the fracture strain after different heat treatments during which the coarse Cr-rich carbides are partially dissolved, although those particles are thought to be preferred nucleation sites for ductile damage. The objective of the paper is to propose a physics based micromechanical analysis, rooted on experimental evidences, to explain this unexpected trend. More importantly, contributing to a better understanding and description of the microstructure-property relationship for this class of martensitic stainless steel should enable the design of microstructure with enhanced mechanical properties.

2. Experimental methods

A modified AISI 410 martensitic stainless steel was continuously cast, hot rolled and cold rolled to 1.5 mm thick plates by Aperam Stainless Steel Europe. The chemical composition is reported in Tab. 1.

Figure 1 shows the as-received microstructure. The steel presents a fully ferritic structure with a mean grain size of $9\mu m$. 1.5 vol.% of $M_{23}C_6$ (M=Fe,Cr) and 0.12 vol.% NbC carbides are dispersed in the matrix phase with $M_{23}C_6$ aligned along the rolling direction (RD).

Computational thermodynamics calculations of carbides volume fraction with the TCFE6 database of Thermo-Calc [39] software program are in very good agreement with experimental results, suggesting that the as-received materials is at thermodynamic equilibrium. During austenization, $M_{23}C_6$ particles partially dissolves in the surrounding matrix. On the contrary, due to their higher thermodynamic stability, NbC are not affected by the heat treatment.

Samples were heat treated at 875°C, 900°C and 975°C for 60, 15 and 5 minutes respectively to transform the ferrite to austenite and partially dissolve the $M_{23}C_6$ particles. These samples were then air-quenched to room temperature at a rate of about 10°C/s. Next, heat treated samples were prepared for

standard microstructure characterization. Each sample was first mechanically ground with SiC papers, then polished down to 1 μm diamond paste followed by a final polishing with a 0.03 μm OPS-A suspension for 30 minutes.

Samples for microstructure characterization were etched with Behara reagent (0.28 g Potassium disulphite, $K_2S_2O_5$, 20ml HCl 37%, 100ml distilled H_2O) for 8 seconds at room temperature and with a modified Murakami's reagent (alkaline $KMnO_4$ at 60°C for 5 minutes). The latter etching technique is known to selectively colour $M_{23}C_6$ carbides [40, 41, 42], which allows quantitative and reproducible characterizations of these particles with standard metallographic techniques. Next, the microstructure was characterized with light optical microscopy (LOM) and scanning electron microscopy (SEM) using both backscattered (BSE) and secondary electrons (SE). Analysis with energy dispersive x-ray diffraction (EDX) in the SEM confirms that etched particles consist of Cr-rich $M_{23}C_6$ carbides. Finally, quantitative image analysis was carried out using the open-source ImageJ software [43] to measure carbides volume fraction and the parameter χ=R/L, defined as the ratio between the mean particles radius, R, and the mean distance between closest neighbour particles, L [44].

Uniaxial tensile tests were performed at a strain rate of 0.1 mm/s on subsized ASTM-E8 samples prepared by electric discharge machining (EDM). The cross-section dimensions are 12.5 mm x 1.5 mm with a total gauge length of 50 mm. Bending tests were performed on 60 mm x 60 mm x 1.5 mm square samples at a strain rate of 0.1 mm/s. A total of 30 samples (10 for each heat treatment) were machined from different regions of the master plate in order to have a good statistical representation of the average properties. Mechanical tests were performed along the rolling direction (RD) of the sheet. In bending, the bending line was aligned perpendicular to RD, therefore producing the main tensile (and compressive) stresses along RD. Bending tests, which better represent the real loading conditions during crash tests, were performed following the "Verband Der Automobilindustrie" (VDA) 238-100 test specification for steel sheet. The damage process was analysed along the longitudinal section and at different distances from the fracture surfaces of post-mortem uniaxial tensile

test samples, which were sectioned at mid-width with a micro cutting machine as schematically shown in Fig. 5. Damages were evaluated on SEM micrographs of unetched specimens by quantitative measurements of void area fraction, void density, void aspect ration and average void size.

Nanoindentation was performed on unstrained samples with a three sided diamond pyramidal tip (E_i=1141 GPa, υ_i=0.07) with an apex angle of 90° using continuous stiffness measurement (CSM) mode. Hardness was probed within individual grains, from which mechanical properties at the macroscale can be discerned [45, 46, 47]. Before nanoindentation, a rectangular area of 50μm x 22.5μm was observed with SEM backscatter electrons in order to identify the phases topology. Then the same area was probed with a matrix of 20 x 10 indentations with an average spacing between indents of δx=δy=2.5μm to ensure no overlapping of plastically deformed imprints. The hardness (H^{true}) at 100 nm indentation depth was calculated with the method proposed by Oliver and Pharr [48] and taking into account the effect of material pile-up. Knowing the true Young modulus (E^{true}= 195 GPa) and the Poisson ratio (υ=0.3) the reduced true modulus E_r^{true} can be calculated with the Sneddon relationship:

$$\frac{1}{E_r^{true}} = \frac{1-\upsilon^2}{E^{true}} + \frac{1-\upsilon_i^2}{E_i} \tag{1}$$

The reduced modulus is also equal to:

$$E_r^{true} = \frac{1\pi S}{\beta 2\sqrt{A}} \tag{2}$$

where S is the measured contact stiffness, β=1 and $A = f(h_c)$ is the contact area derived from preliminary tip calibration function. Equations 1 and 2 can be combined with the definition of hardness, $H = P/A$ (with P equal to the measured load), to get rid of the contact area and find the true value of hardness (H^{true}), which cancels out the effect of material pile-up:

$$H^{true} = \frac{P}{A}(\beta\frac{2}{\sqrt{\pi}}\frac{\sqrt{A}}{S})^2 = \frac{P}{S^2}\frac{4\beta^2}{\pi}(E_r^{true})^2 \tag{3}$$

3. Results

3.1. Microstructures after heat treatment

Figure 2(a-c) shows the sample's microstructure after heat treatments at 875°C (Fig. 2a), 900°C (Fig. 2b) and 975°C (Fig. 2c). These produce microstructure consisting of 85vol % martensite and 15vol % of ferrite, while chromium carbides initially present in the microstructure are increasingly dissolved at higher temperatures. Table 2 provides the volume fraction, mean size and the parameter χ of the residual $M_{23}C_6$ carbides after the three heat treatments. When the austenization temperature is increased above the carbide solvus temperature of 868°C, the volume fraction, mean size and parameter χ of carbides all decrease.

3.2. Mechanical tests

Figure 3 shows the results of the bending and uniaxial tensile tests performed after the three heat treatment conditions. The two loading mode lead to the same trend. Increasing the heat treatment temperature slightly increases the strength while the uniform elongation (Fig. 3b) and the bending angle at maximum load (Fig. 3a) are reduced. Figure 4 shows the fracture strain, measured on post-mortem fracture surfaces and the bending angle at crack initiation as a function of χ. Ductility decreases for higher austenization temperatures. This indicates that higher ductility can be achieved even though the particles are coarser and more closely spaced. This contradicts expectations, as discussed in the introduction. Table 3 summarises the mechanical properties measured by tensile and bending tests after the three different heat treatments. The effect is significant, with a reduction of ductility by more than 10% in the microstructure containing the lowest volume fraction of $M_{23}C_6$.

3.3. Damage characterization

Damage nucleates and grows at primary and secondary population of carbides, through either carbide interface debonding or particle cleavage. While

the former is certainly more commonly observed, the latter mechanism is also present. At low strain, damage preferentially nucleates at coarse $M_{23}C_6$ particles: Fig. 6 shows partial decohesion between a $M_{23}C_6$ carbide and the surrounding ferrite matrix. At high strain, damage nucleates at both $M_{23}C_6$ and nano-sized NbC carbides. The latter nucleation process is only observed in the close proximity of the fracture surfaces and is believed to trigger the final void coalescence process.

Figure 7 shows the void area fraction variation with deformation in uniaxial tension specimens. While the initial porosity is equal to 0.02 area % and similar for the three austenization conditions, the damage evolution is substantially different. The void area fraction at a true strain of $\epsilon_{true} = 0.6$ is three times larger for samples heat treated at 975°C. To further analyse the damage evolution, voids were divided in two classes of size. Voids smaller than 100 nm were considered as newly nucleated voids, while larger voids were treated as growing voids. The area fraction evolution for the two void populations is shown in Fig. 7. Large voids make up most of the void area fraction for all three heat treatments. The void density can be separated on the same basis as shown in Figs. 8a and 8b. The density of both small and large voids increases with strain, which indicates a continuous void nucleation process on the carbides. The density of nano-sized voids suddenly increases above $\epsilon_{true} = 0.4$. This corresponds to nucleation events occurring at NbC particles, which eventually promotes the final void coalescence process. This increment in density and volume fraction of nano-sized voids is mainly observed after the 975°C heat treatment. Next, the voids aspect ratio evolution shown in Fig. 9b indicates a strong elongation along the tensile direction for the largest voids. On the other hand, the aspect ratio of voids below 100 nm (Fig. 9a) remains constant throughout deformation.

3.4. Fracture morphology

Uniaxial tension specimens exhibit a slant fracture profile, typical of high strength steel sheets. The analysis of fracture surfaces confirms a fully ductile process. It displays two populations of dimples, which can be related to nucle-

ation at the $M_{23}C_6$ and NbC carbides respectively. Figure 10 shows a typical fracture surface of a uniaxial tension specimen. Large dimples, which nucleated at coarse $M_{23}C_6$ particles, are bridged by a second population of nano-sized dimples which originated from NbC particles. This mechanism is clearly visible in Fig. 10(b).

3.5. Nanoindentation

Nanoindentation indicates that the different heat treatments affect the strength of both ferrite and martensite. Figures 11(a-c) show a partial view of the nanohardness contour maps as measured by the nanoindentation test after the heat treatment. The mechanical strength contrast, visualized by the "peaks" and "valleys" in Fig. 11(a-c), steadily increases with higher austenization temperatures. This is the result of carbide dissolution, which increases the amount of alloying elements in solid solution. Due to the greater carbon solubility in austenite, this element will mainly be found in martensite after quenching, which greatly increases its strength. Fig. 11(d) shows the hardness distribution in the martensite grains. The average strength of this phase is increased owing to a higher carbon content. Moreover, in the martensite produced by the heat treatment at 975°C, there is an increasing number of martensite grains with particularly high strength (larger than 4 GPa). Table 4 summarizes average hardness of the ferrite and martensite phases, which increases of 3% and 7%, respectively.

4. Model

4.1. Description of identific of the FE model

Finite element (FE) simulations were performed in order to investigate the plastic strain distribution among ferrite and martensite grains under uniaxial tension conditions. A 3D distribution of ferrite and martensite grains was generated through a Python algorithm, which randomly distributed 15vol % of ferrite grains inside the martensite matrix (85 vol.%). The FE mesh had a total size of

30^3 cubic elements with linear interpolation (C3D8 in Abaqus). Each cube was associated to a ferrite or a martensite grain (Fig. 12a). Such mesh refinement allows probing the heterogeneities of stress triaxiality and plastic strain, which constitute two important indicators of damage evolution. Periodic boundary conditions were enforced to avoid artefacts at the edges of the FE mesh and isotropic J_2 plasticity was assumed throughout the simulation. Ferrite flow behaviour was modelled by fitting a Voce law on the experimental flow curve of the material before austenization:

$$\sigma_\alpha = \sigma_{sat} - (\sigma_{sat} - \sigma_{y0})exp(-a\epsilon_p) \tag{4}$$

where σ_{y0}= 270 MPa is the experimental yield strength of ferrite; σ_{sat}= 620 MPa and a=15 are fitting parameters; ϵ_p is the accumulated equivalent plastic strain.

The yield strength of martensite was adjusted as a function of the carbon content by fitting the following equations to match the experimental flow curves:

$$\sigma_y[MPa] = 760 + 6200(wt\%C - 0.1) \tag{5}$$

The strain hardening behaviour of martensite is usually sensitive to its carbon content [49, 50]. However, in the three microstructures here produced, the small difference of carbon content does not substantially change their strain hardening. This assumption is supported by the uniaxial tensile test results in Fig. 3(a), which show no difference in strain-hardening between the three heat treated microstructures.

4.2. FE simulations of the DP microstructure

Figure 12b shows the experimental engineering stress-strain (solid lines) and predicted (discrete symbols) curves for the three heat treatment conditions. The agreement is quite good justifying the choices made for the phase properties. The simulation is not able to predict the post necking response due to the imposed periodic boundary conditions (preventing necking to develop) as well as the absence of damage induced softening in the constitutive model.

Figure 13 shows the two cumulative distributions of stress triaxiality (13a) and plastic strain (13b) values in ferrite and martensite. At similar macro-strain the stress triaxiality and plastic strain in ferrite both increase with increasing mechanical strength contrast. On the contrary, the distribution of these two parameters in martensite is not sensitive to the different heat treatment conditions.

As plastic strain and stress triaxiality are both critical parameters for damage growth [35], a simple damage indicator D based on the Rice and Tracey void growth model [51] is defined:

$$D = \int_0^{\epsilon} e^{\frac{\sigma_m}{\sigma}} d\epsilon \tag{6}$$

where σ_m is the mean (or hydrostatic) stress, σ the equivalent Von Mises stress and ϵ the accumulated plastic strain. Figs. 14(a) and (b) show the cumulative distributions of D in ferrite and martensite computed for ϵ= 0.05, 0.2, 0.3 and 0.4. The distribution among the ferrite grains is modified by the heat treatments. The driving force for damage accumulation as quantified by D is significantly enhanced when increasing phase mechanical contrast, i.e. increasing austenization temperature. This comes from the combined effect of stress triaxiality and plastic strain previously shown in Figs. 13 (a) and (b).

Figure 15 shows the average computed phase configuration around the hot-spot. This is calculated with a method recently described in [36] and here briefly recalled. The damage indicator D introduced in Eq. (6) is known at every position of the tridimensional space $D(i, j, k)$. Next, an indicator, P, marks if at a certain position i, j, k belongs to martensite or ferrite. Finally, the average phase configuration around the damage initiation hot-spot is described by:

$$P_D(\Delta i, \Delta j, \Delta k) = \frac{\sum_{i,j,k} D(i,j,k) P(i+\Delta i, j+\Delta j, k+\Delta k)}{\sum_{i,j,k} D(i,j,k)} \tag{7}$$

in which $(\Delta i, \Delta j, \Delta k)$ indicates the relative position with respect to the damage hot-spot and $\sum_{i,j,k}$ is looped for all grains in the simulation domain. Equation (7) gives the probability to find martensite (and consequently ferrite) around the

damage initiation sites. Figure 15 shows in blue the relative positions where the probability P_D is larger than the nominal martensite volume fraction ($V_{\alpha'} \leq P_D(\Delta i, \Delta j, \Delta k) \leq 1$). While the colour red is used to indicate that there is greater chance to find ferrite at this position relative to damage sites ($0 \leq P_D(\Delta i, \Delta j, \Delta k) \leq V_{\alpha'}$).

Most damage hot-spots are found in the ferrite phase and are enclosed by two regions of martensite. This particular microstructure configuration is found to be critical for damage initiation. Moreover, the three dimensional view in Fig. 15 reveals that the damage hot-spot tends to be surrounded by a flat toroid of ferrite grains perpendicular to the main tensile direction.

5. Discussion

As briefly overviewed in the introduction and shown in Fig. 6, $M_{23}C_6$ carbides constitute the primary sites of damage initiation in the present martensitic-ferritic stainless steel. Decreasing the area void fraction and mean size of such nucleation sites was thus expected to improve the resistance to ductile damage nucleation with consequent beneficial effect on the overall ductility [52], [33], [53]. On the contrary, the experimental evidences summarized in Tab. 3 indicate a diminution of ductility even if the void area fraction and mean size of $M_{23}C_6$ carbides decreases.

Higher austenization temperature decreases the equilibrium volume fraction of $M_{23}C_6$ carbides, thus increasing the carbon content in the surrounding austenite. Thus, martensite that forms upon quenching from higher austenization temperatures is characterized by higher hardness and corrosion resistance thanks to the dissolved C and Cr, respectively.

The martensite carbon content can be estimated using Thermo-Calc software with an equilibrium calculation between the austenite matrix and the residual volume fraction of $M_{23}C_6$ and NbC carbides. The strength increment due to the carbon enrichment in low-carbon lath martensite can then be predicted based on empirical equations. From Krauss [2] the effect of carbon in solid solution in

martensite can be written as:

$$\sigma_y[MPa] = 413 + 1720\sqrt{[wt\%C]} \tag{8}$$

Moreover, Cr is found to contribute to the yield strength of martensite by 30 MPa for every 5wt % of Cr dissolved in the matrix [54]. The strength of martensite as a function of carbon content according to Eq. (13) together with the measured hardness values from nanoindentation are listed in Tab.5. Both methods result in an increase of martensite strength of about 7% which confirms that the strength increment detected by nanoindentation mapping is essentially due to the larger amount of carbon in solid solution in the martensite lattice. On the other hand ferrite is not strengthened during the dissolution process, which consequently raises the mechanical strength contrast between the two phases.

The presence of residual ferrite has a large effect on ductility. The computational modelling results presented in Fig. 13 show high values of plastic strain and stress triaxiality in ferrite as the mechanical strength contrast increases. These conditions have been known to promote the void nucleation and growth process in ductile metallic materials [35] and more specifically in dual-phase steels [23, 19], [36, 37], [45, 55, 56, 27, 21, 22, 26]. The damage indicator described in Eq. (6) and plotted in Fig. 14 qualitatively agrees with the characterization of the damage evolution shown in Fig. 7. Higher austenization temperatures produce microstructure with larger mechanical strength contrast, which leads to high stress triaxiality in the ferrite phase. This particular situation enhances the void growth rate in the ferrite grains, leading to the premature failure of the material. These results, other than highlight the detrimental effect of residual ferrite on the ductility of MSS, contribute to the understanding of the recent finding by Jo et al. [57], which highlights the negative effect of residual ferrite on impact toughness of Hot-Press-Forming (HPF) steel sheets.

In the finite element simulations performed here, each grain was represented with a single cubic element, which was assigned systematically to ferrite or martensite phase with unique mechanical properties. In reality, the nanoindentation maps shown in Figs. 11(a-c) revealed a much complex heterogeneity of

strength among the microstructure. One might expect, for example, that relying on a more realistic grain shapes and a more refined mesh would increase the predicted strain heterogeneity. Indeed, simulations performed with grains shaped as truncated octahedron have shown stress triaxiality 2.5 times larger than the macroscopic value was observed in ferrite [58]. In the same study, ferrite clustering was also found to have limited influence on strain partitioning and on the stress triaxiality values.

Finally, the topology of ferrite and martensite grains was found to significantly impact damage initiation. The phase configuration, shown in Fig. 15, indicates that the morphology and dispersion of ferrite islands have both a considerable impact on the mechanical properties of the alloy. Even though the ratio of ferrite to martensite is reversed, there is a similarity among the critical phase configuration between this work previous similar observations of damage hot-spot in DP steels [37]. However, contrary to the mentioned work where the phase configuration was assessed in two dimensions only, the three dimensional phase configuration shown in Fig. 15 (a) reveals that percolation of ferrite grains perpendicular to the tensile direction promotes damage initiation.

The present finding is also reminiscent of the problem found in austenite-ferrite steels where the increased triaxiality in the soft phase was due to a channel type configuration of the microstructure [38, 59, 60]. In any case, the present study reveals that the key factor controlling the fracture process in two phases ductile steel is not necessarily the concentration of damage initiation sites (here carbides) but could primarily be the state of stress in the softer phase inside which damage grows.

6. Conclusion

The damage mechanisms occurring in a martensitic stainless steel with 15 vol.% of residual ferrite and two populations of carbides has been investigated both experimentally and numerically. Damage initiates at coarse Cr-rich carbides in ferrite grains. However, dissolution of these particles leads to a decrease of the ductility. The origin of the lower ductility in the alloy with less Cr-rich carbides was unravelled through nanoindentation strength mapping and FE simulations of representative volume elements. The main findings are:

- The dissolution of Cr-rich carbides increases the carbon content of martensite, producing a relative strength increment of about 7 %.
- The mechanical strength contrast between martensite and residual ferrite increases with increasing carbides dissolution at higher austenization temperatures.
- FE simulations predict an increasing stress triaxiality in the ferrite grains as the mechanical strength contrast increases. This promotes void growth in ferrite, which in turn decreases fracture strain.
- A statistical study of FE simulations reveals that there is a critical phase configuration that maximizes damage. Voids are more likely to initiate in channels of percolated ferrite aligned perpendicular to the main tensile direction. These features are highly constrained by surrounding martensite.

The stress triaxiality and plastic strain can rise a lot (i) when mechanical contrast increases and (ii) in specific phase configuration. These are two elements that must be kept in mind when optimizing existing alloys or developing new ones. One practical way to eliminate mechanical stress contrast is to produce single matrix phase structure. In MSS this can be achieved by a complete austenization before quenching. However, this requires a deep knowledge of the transformation kinetics and it is not always possible to attain when taking into account the constraints dictated by the standard industrial process conditions.

7. Acknowledgement

The authors thank Professor Anne-Francoise Gourgues-Lorenzon and Helene Godin, Ecole Nationale Superiore des Mines de Paris (MINES ParisTech) for fruitful discussions. The financial support of CBMM (Companhia Brasileira de Metalurgia e Mineracao) is acknowledged. A. Miotti Bettanini also thanks Sophie Ryelandt, UCL, for carrying out the nanoindentation measurements that resulted in Fig.11. L. Delannay is mandated by the FNRS-Belgium.

8. Tables

Table 1: Chemical composition of the as-received alloy (*wt.%*).

C	Cr	Si	Mn	Ni	Nb	V	P	Cu	Fe
0.1	12	0.4	0.35	0.1	0.1	0.08	0.02	0.04	Bal.

Table 2: Volume fraction, mean size and the distribution parameter χ=R/L of $M_{23}C_6$ for the three heat treatment conditions.

Heat Treat.	$M_{23}C_6$ Vol.%	$M_{23}C_6$ (μm)	χ
875°C, 60 min	0.5	0.35	0.1158
900°C, 15 min	0.3	0.28	0.0927
975°C, 5 min	0.1	0.24	0.0829

Table 3: Mechanical properties for the three heat treatments conditions measured with uniaxial tensile and bending tests. Ductility as quantified by true fracture strain or bending angle decreases together with the austenization temperature.

Processing Temperature	σ_0 (MPa)	ϵ_f	Bending Angle (°)
875°C, 60 min	721	0.90	91
900°C, 15 min	814	0.83	85
975°C, 5 min	834	0.81	73

Table 4: Average hardness of martensite ($H_{\alpha'}$) and ferrite (H_α) measured by nanoindentation. The carbide volume fraction and ferrite volume fraction for the three austenization conditions are also reported.

Heat Treat.	$M_{23}C_6$ Vol.%	α(Vol.%)	$H_{\alpha'}^{true}$(GPa)	H_α^{true}(GPa)
875°C, 60 min	0.5	15.0	3.36	2.29
900°C, 15 min	0.3	15.4	3.46	2.30
975°C, 5 min	0.1	15.0	3.61	2.34

Table 5: Carbon content in martensite from Thermo-Calc calculations, martensite hardness values and martensite yield strength according to Krauss empirical relationship [2].

Heat Treat.	Cα'(wt%)	$H_{\alpha'}^{true}$(GPa)	$\sigma_y^{\alpha'}$(MPa)[2]
875°C, 60 min	0.076	3.36	889
900°C, 15 min	0.085	3.46	915
975°C, 5 min	0.097	3.61	950

9. Figures

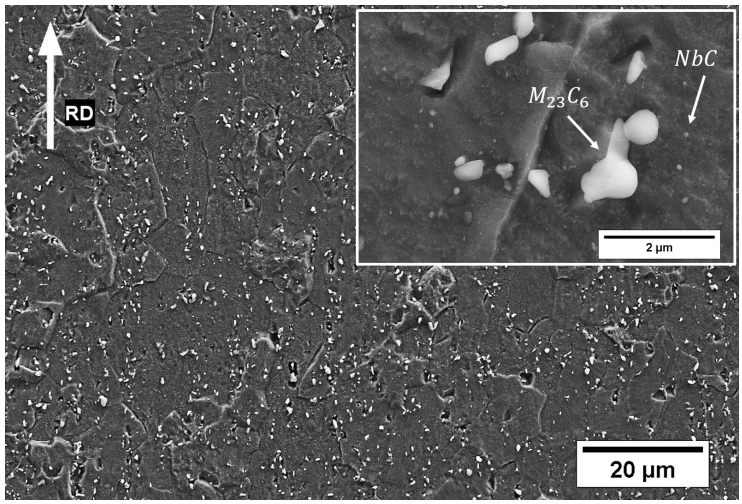

Figure 1: The as-received material microstructure, which, after casting and hot rolling, consists of ferrite and $M_{23}C_6$ particles aligned towards RD. The magnification shows $M_{23}C_6$ and NbC particles.

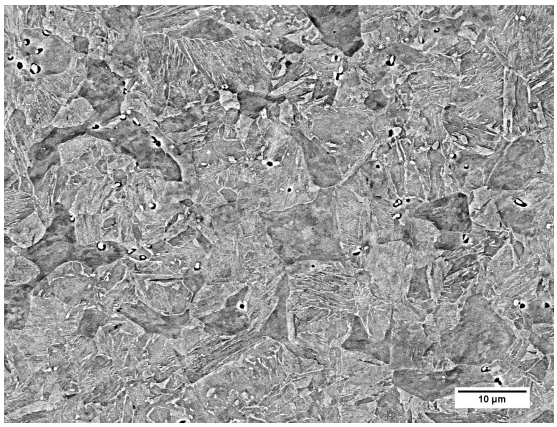

(a)

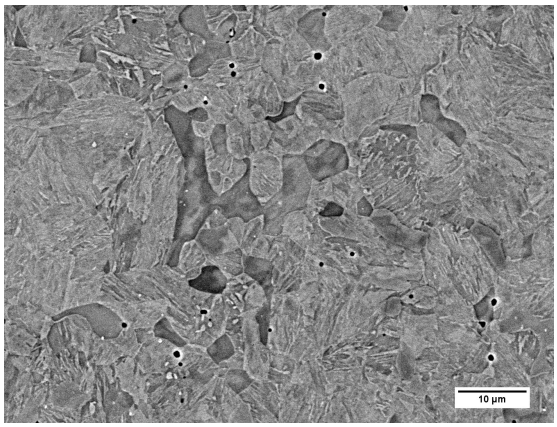

(b)

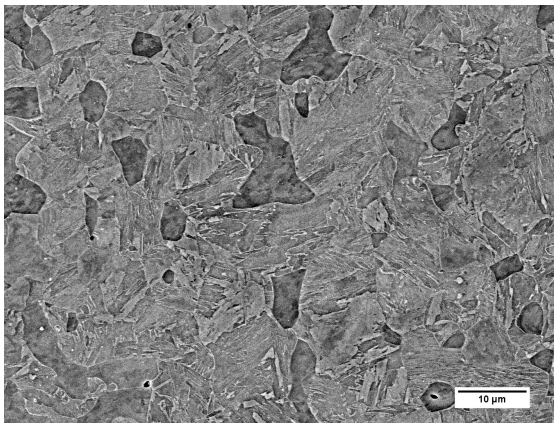

(c)

Figure 2: Typical microstructure after the heat treatments for a)875°C 60 min, b)900°C 15 min and c)975°C 3 min. Note the presence of 5 Vol.% of residual ferrite and coarse $M_{23}C_6$ particles.

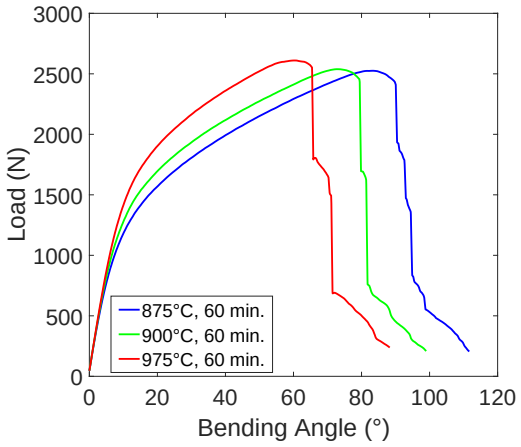

(a)

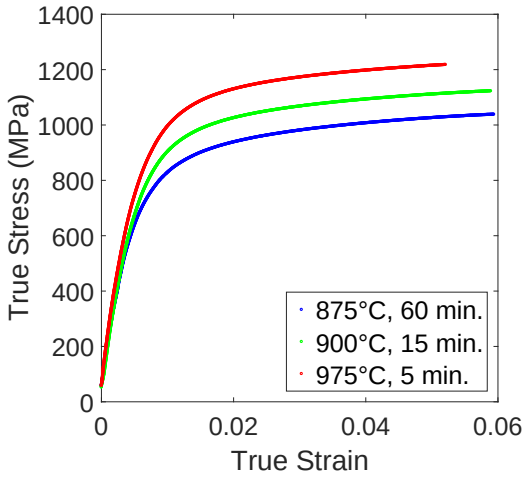

(b)

Figure 3: The experimental curves for bending test (a) and uniaxial tensile test (b) for the three heat treatment conditions. The colors represent different austenization temperatures.

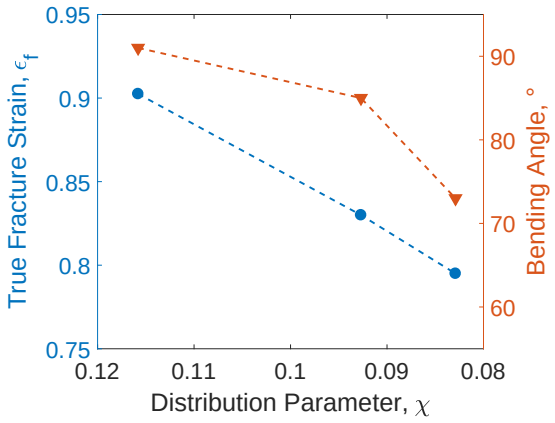

Figure 4: Variation of the true fracture strain as a function of the ratio χ between the mean particle radius and closest neighbour distance, the fracture strain and bending angle both decrease with decreasing χ.

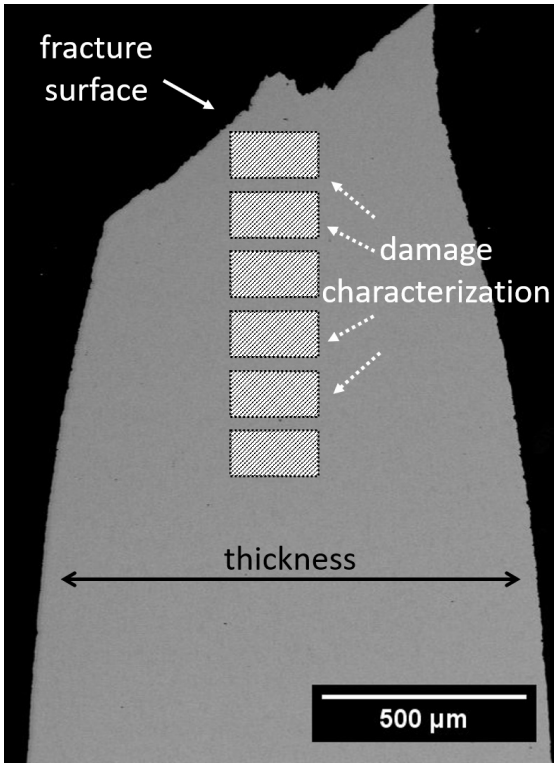

Figure 5: Micrograph showing the position of the regions in which the damage has been quantified in transverse sections located at different distances from the fracture surface. Each region was mapped using several high magnification SEM images.

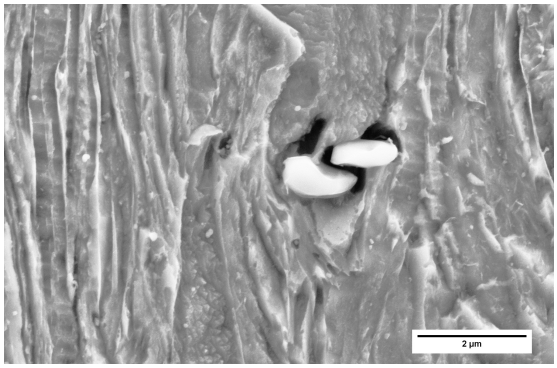

(a)

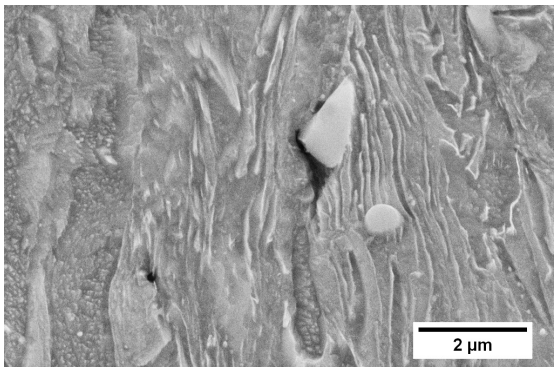

(b)

Figure 6: SEM micrographs of damage nucleation events occurring at $M_{23}C_6$ carbides either (a) by carbide cleavage or (b) by decohesion of the carbide from the matrix.

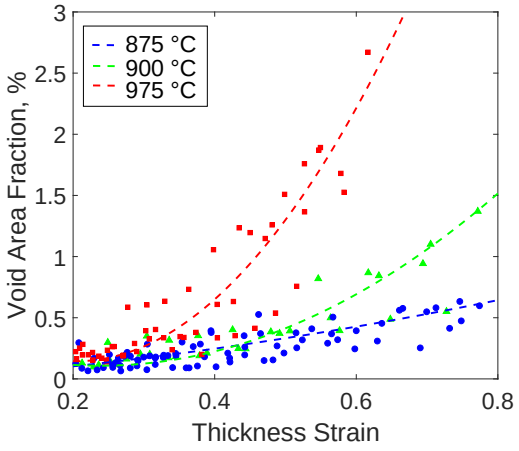

(a)

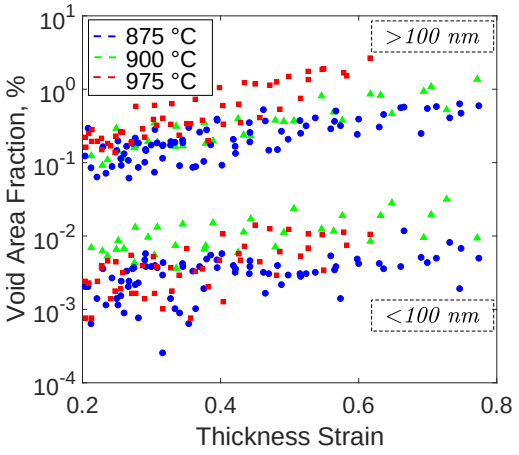

(b)

Figure 7: Variation of the void area fraction of the two void populations corresponding to the three heat treatments as a function of the local deformation (from thickness reduction); (a) all voids together; (b) when separating voids into two class sizes, $<$ or $>$ 100 nm.

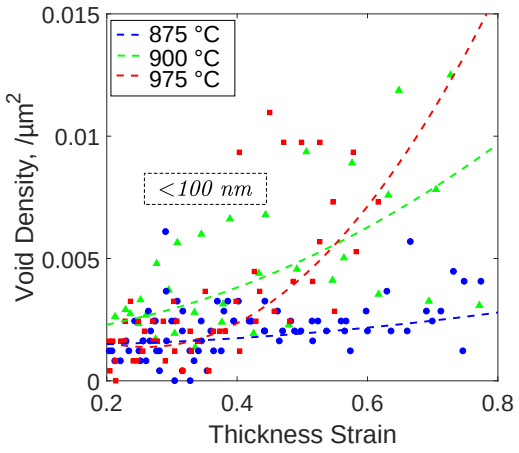

(a)

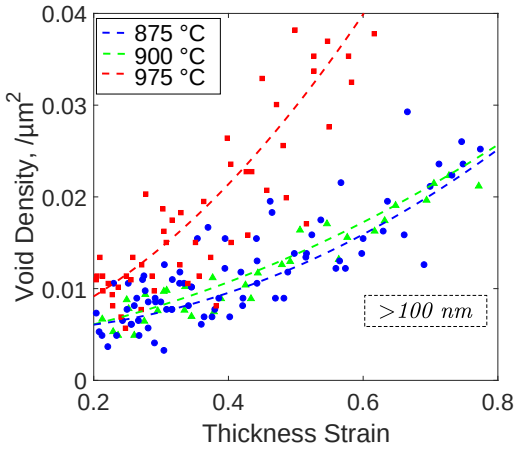

(b)

Figure 8: Variation of average voids density; (a) for the group of voids < 100 nm; (b) for the group of voids > 100 nm as a function of the local deformation (from thickness reduction).

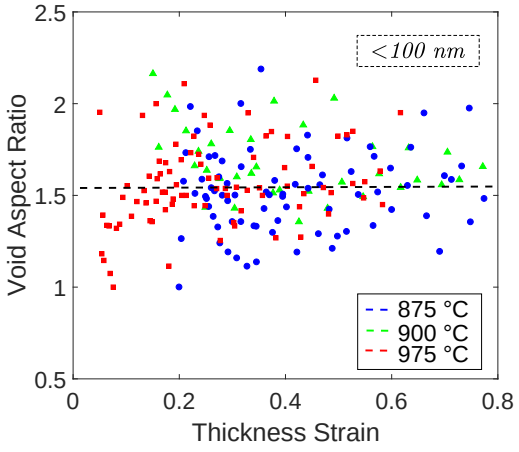

(a)

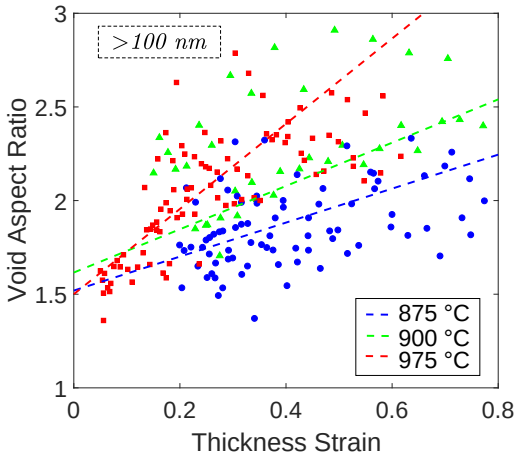

(b)

Figure 9: Variation of the average voids aspect ratio (AR); (a) for the group of voids < 100 nm; (b) for the group of voids > 100 nm as a function of the local deformation (estimated from thickness reduction).

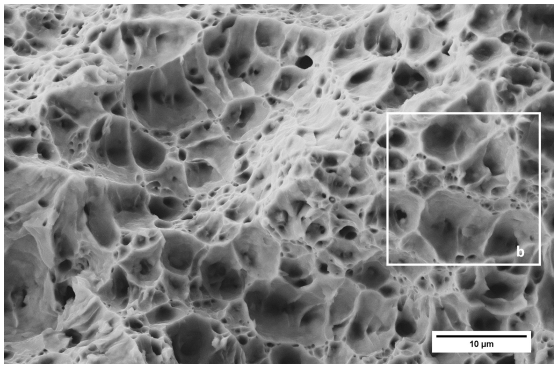

(a)

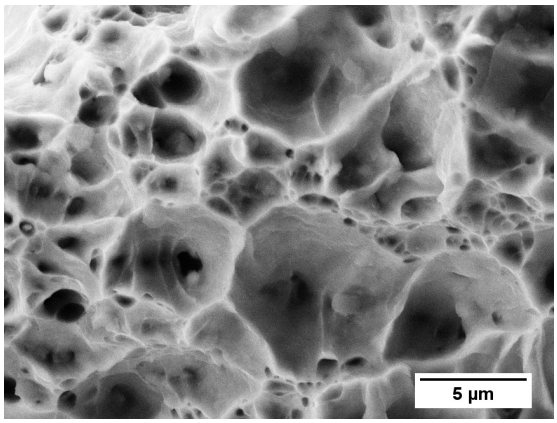

(b)

Figure 10: SEM images showing ductile fracture from tensile samples at (a) low magnification and (b) higher magnification showing two populations of dimples, with nano-sized dimples linking larger cavities.

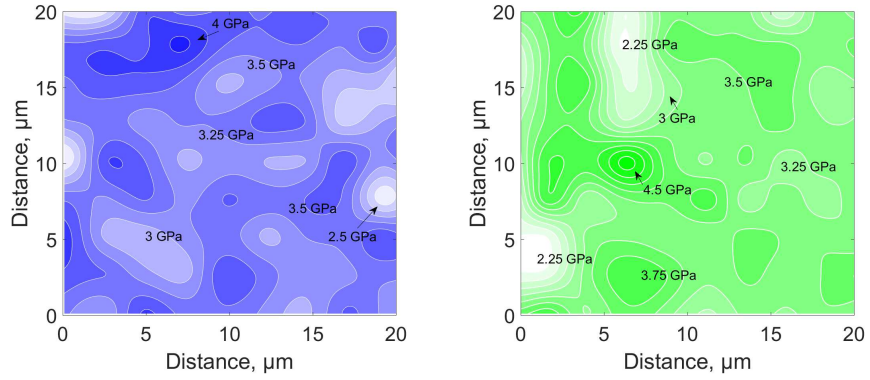

(a) *875° C, 60 minutes.*

(b) *900° C, 15 minutes.*

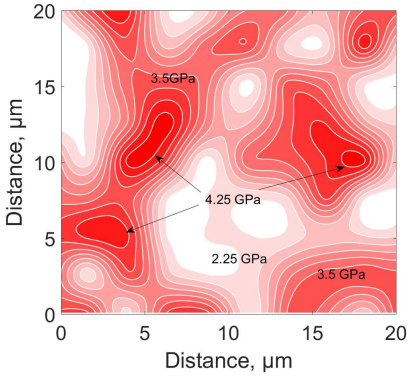

(c) *975° C, 5 minutes.*

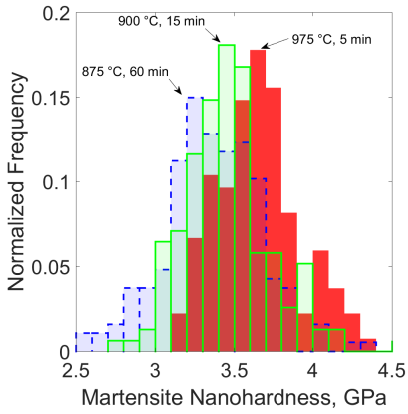

(d)

Figure 11: Nanohardness (H^{true}) contour maps of the dual-phase microstructures heat treated at (a) 875°C 60 min, (b) 900°C 15 min and (c) 975°C 5 min. (d) shows the hardness distribution in the martensite grains only for the three heat treatments.

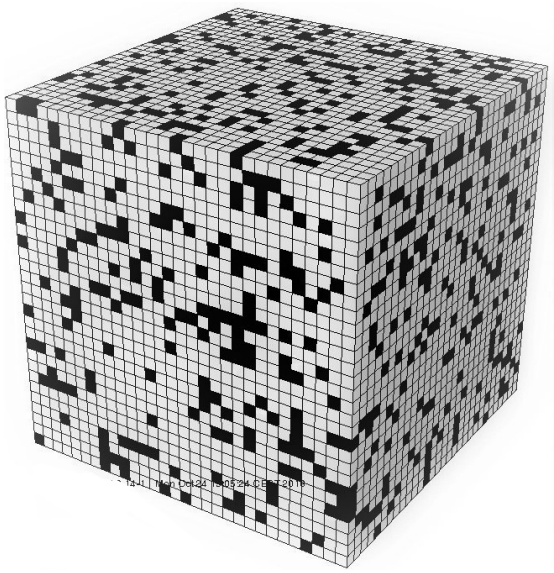

(a)

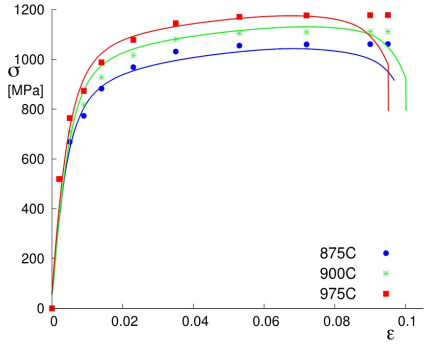

(b)

Figure 12: FE simulations; (a) 3D FE mesh with random configuration of ferrite grains, in black, inside the martensite scaffold (grey); (b) experimental engineering stress-strain curves (solid lines) and FE model prediction (symbols).

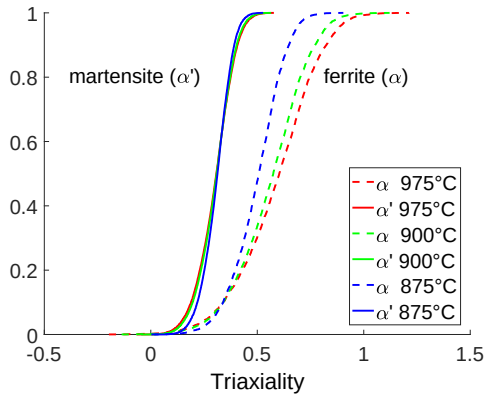

(a)

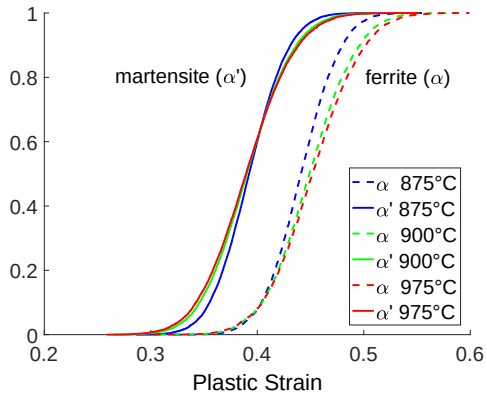

(b)

Figure 13: Cumulative distributions of a) stress triaxiality and b) plastic strain values inside the ferrite and martensite phases for the three heat treatments at a macroscopic equivalent strain ϵ=0.4.

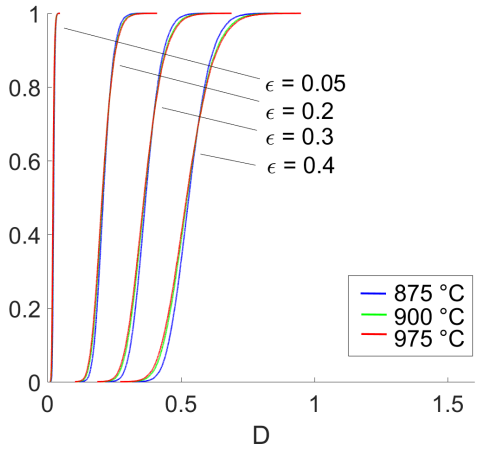

(a) *Martensite.*

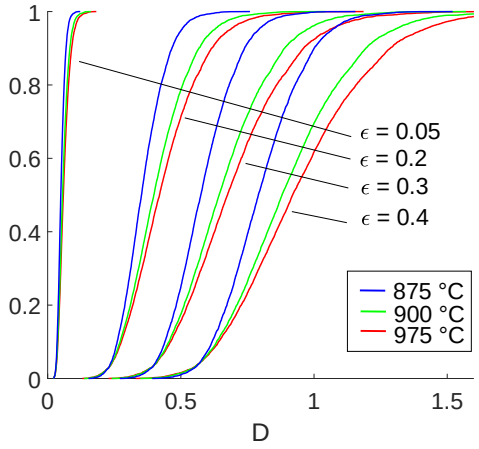

(b) *Ferrite.*

Figure 14: Cumulative distribution of the damage indicator values D in martensite (a) and ferrite (b) for the three heat treatments at a macroscopic equivalent strain ϵ= 0.05, 0.2, 0.3, 0.4. The impact of the heat treatment on the phase properties reflects on significant variation in the damage process in ferrite.

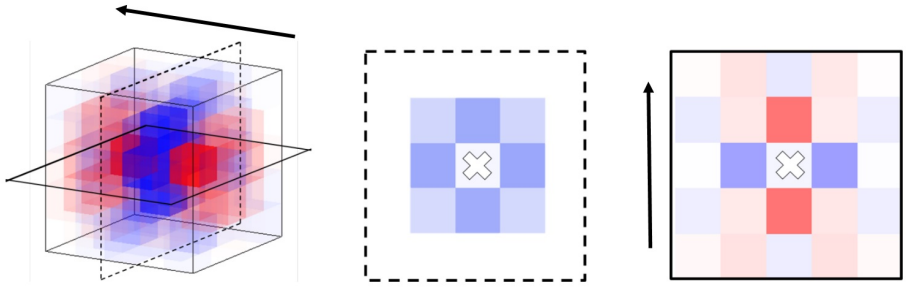

Figure 15: Calculated configuration of phases around a hot-spot. Ferrite (blue) island is enclosed between two regions of martensite (red). The arrow indicates the displacement direction (tensile direction in uniaxial deformation).

10. References

[1] D. S. Codd, Automotive Mass Reduction with Martensitic Stainless Steel, SAE International, 2011, pp. 2011–01–0427.

[2] G. Krauss, Martensite in steel: strength and structure, Materials Science & Engineering A 273-275 (1999) 40–57. doi:10.1016/S0921-5093(99)00288-9.

[3] G. Krauss, Deformation and Fracture in Martensitic Carbon Steels Tempered at Low Temperatures, Metallurgical and Materials Transactions A 32B (2001) 1–17.

[4] F. Ruel, P.-O. Santacreu, S. Saedlou, G. Badinier, J. Herbelin, Corrosion Aspects Regarding the Use of Martensitic Stainless Steels in Automotive Chassis Parts, SAE International, 2015, pp. 2015–01–1347. doi:10.4271/2015-01-1347.

[5] P.-O. Santacreu, G. Badinier, J.-B. Moreau, J.-M. Herbelin, Fatigue Properties of a New Martensitic Stainless Steel for Hot Stamped Chassis Parts, SAE International, 2015, pp. 2015–01–0527. doi:10.4271/2015-01-0527.

[6] G. Badinier, J. D. Mithieux, Relation microstructure-propriétés mécaniques d'un acier martensitique inoxydable, MATEC Web of Conference 7 (01012).

[7] A. J. Deardo, Niobium in modern steels, International Materials Reviews 48 (2003) 371–402. doi:10.1179/095066003225008833.

[8] D. Kalish, M. Cohen, Structural changes and strengthening in the strain tempering of martensite, Materials Science and Engineering 6 (1970) 156–166. doi:10.1016/0025-5416(70)90045-5.

[9] R. Honeycombe, H. K. D. H. Bhadeshia, Steel Microstructure and Properties, Elsevier, 2010.

[10] C. G. de Andrés, G. Caruana, L. F. Alvarez, Control of M 23 C 6 carbides in 0.45 C–13Cr martensitic stainless steel by means of three representative heat treatment parameters, Materials Science & Engineering A 241 (1998) 211–215. doi:10.1016/S0921-5093(97)00491-7.

[11] S. Kou, Welding Metallurgy, John Wiley & Sons, 2003.

[12] E. M. Westin, Microstructure and properties of welds in the lean duplex stainless steel ldx 2101, Ph.D. thesis, KTH, Physical Metallurgy, qC 20101213 (2010).

[13] C. Liu, Y. Liu, D. Zhang, B. Ning, Z. Yan, Effect of M3C on the Precipitation Behavior of M23C6 Phase during Early Stage of Tempering in T91 Ferritic Steel, Steel Research Int. 82 (2011) 1362–1367. doi:10.1002/srin.201100153.

[14] C. Garcia, L. F. Alvarez, M. Carsi, Effects of heattreatment parameters on nonequilibrium transformations and properties of X45Cr13 and X60Cr14MoV martensitic stainless steels, Welding International 6 (1992) 612–621. doi:10.1080/09507119209548251.

[15] A. Bojack, L. Zhao, P. F. Morris, J. Sietsma, Austenite Formation from Martensite in a 13Cr6Ni2Mo Supermartensitic Stainless Steel, Metallurgical and Materials Transactions A 47 (2016) 1996. doi:10.1007/s11661-016-3404-z.

[16] G. R. Speich, V. A. Demarest, R. L. Miller, Formation of Austenite During Intercritical Annealing of Dual-Phase Steels, Metallurgical Transactions A 12 (1981) 1419. doi:10.1007/bf02643686.

[17] R. Wei, M. Enomoto, R. Hadian, H. S. Zurob, G. R. Purdy, Growth of austenite from as-quenched martensite during intercritical annealing in an Fe–0.1C–3Mn–1.5Si alloy, Acta Materialia 61 (2013) 697–707. doi:10.1016/j.actamat.2012.10.019.

[18] Z.-D. Li, G. Miyamoto, Z.-G. Yang, T. Furuhara, Kinetics of Reverse Transformation from Pearlite to Austenite in an Fe-0.6Masspct C Alloy and the Effects of Alloying Elements, Metallurgical and Materials Transactions A 42 (2010) 1586–1596.

[19] C. C. Tasan, M. Diehl, D. Yan, M. Bechtold, F. Roters, L. Schemmann, C. Zheng, N. Peranio, D. Ponge, M. Koyama, K. Tsuzaki, D. Raabe, An Overview of Dual-Phase Steels: Advances in Microstructure-Oriented Processing and Micromechanically Guided Design, Annual Review of Materials Research 45 (2015) 391–431. doi:10.1146/annurev-matsci-070214-021103.

[20] H. Ghadbeigi, C. Pinna, S. Celotto, Failure mechanisms in DP600 steel: Initiation, evolution and fracture, Materials Science & Engineering A 588 (2013) 420. doi:10.1016/j.msea.2013.09.048.

[21] H. Ghadbeigi, C. Pinna, S. Celotto, J. R. Yates, Local plastic strain evolution in a high strength dual-phase steel, Materials Science & Engineering A 527 (2010) 5026. doi:10.1016/j.msea.2010.04.052.

[22] Q. Han, A. Asgari, P. D. Hodgson, N. Stanford, Strain partitioning in dual-phase steels containing tempered martensite, Materials Science and Engineering a-Structural Materials Properties Microstructure and Processing 611 (2014) 90–99. doi:10.1016/j.msea.2014.05.078.

[23] C. C. Tasan, J. P. M. Hoefnagels, M. Diehl, D. Yan, F. Roters, D. Raabe, Strain localization and damage in dual phase steels investigated by coupled in-situ deformation experiments and crystal plasticity simulations, International Journal of Plasticity 63 (2014) 198–210. doi:10.1016/j.ijplas.2014.06.004.

[24] F. Maresca, V. G. Kouznetsova, M. G. D. Geers, Deformation behaviour of lath martensite in multi-phase steels, Scripta Materialia 110 (2016) 74–77. doi:10.1016/j.scriptamat.2015.08.004.

[25] M. Delince, P. Jacques, T. Pardoen, Separation of size-dependent strengthening contributions in fine-grained Dual Phase steels by nanoindentation, Acta Materialia 54 (2006) 3395–3404. doi:10.1016/j.actamat.2006.03.031.

[26] A. P. Pierman, O. Bouaziz, T. Pardoen, P. J. Jacques, L. Brassart, The influence of microstructure and composition on the plastic behaviour of dual-phase steels, Acta Materialia 73 (2014) 298–311. doi:10.1016/j.actamat.2014.04.015.

[27] J. Kang, Y. Ososkov, J. Embury, D. Wilkinson, Digital image correlation studies for microscopic strain distribution and damage in dual phase steels, Scripta Materialia 56 (2007) 999–1002. doi:10.1016/j.scriptamat.2007.01.031.

[28] G. Avramovic-Cingara, C. A. R. Saleh, M. K. Jain, D. S. Wilkinson, Void Nucleation and Growth in Dual-Phase Steel 600 during Uniaxial Tensile Testing, Metallurgical and Materials Transactions A 40 (2009) 3117–3127. doi:10.1007/s11661-009-0030-z.

[29] C. Landron, O. Bouaziz, E. Maire, J. Adrien, Characterization and modeling of void nucleation by interface decohesion in dual phase steels, Scripta Materialia 63 (2010) 973–976. doi:10.1016/j.scriptamat.2010.07.021.

[30] Q. Lai, O. Bouaziz, M. Gouné, L. Brassart, M. Verdier, G. Parry, A. Perlade, Y. Bréchet, T. Pardoen, Damage and fracture of dual-phase steels: Influence of martensite volume fraction, Materials Science & Engineering A 646 (2015) 322–331. doi:10.1016/j.msea.2015.08.073.

[31] D. Kwon, R. J. Asaro, A Study of Void Nucleation, Growth, and Coalescence in Spheroidized 1518 Steel, Metallurgical Transactions A 21A (1990) 117–134.

[32] D. Chae, D. A. Koss, Damage accumulation and failure of HSLA-100 steel,

Materials Science & Engineering A 366 (2004) 299–309. doi:10.1016/j.msea.2003.08.040.

[33] J. G. Cowie, F. R. Tuler, The influence of second-phase dispersions on shear instability and fracture toughness of ultrahigh strength AISI 4340 steel, Materials Science & Engineering A A141 (1991) 23–37.

[34] T. B. Cox, J. R. Low, An investigation of the plastic fracture of AISI 4340 and 18 Nickel-200 grade maraging steels, Metallurgical Transactions 5 (1974) 1457. doi:10.1007/bf02646633.

[35] A. Pineau, A. A. Benzerga, T. Pardoen, Failure of Metals I – Brittle and Ductile Fracture, Acta Materialia 107 (2016) 424–483. doi:10.1016/j.actamat.2015.12.034.

[36] T. W. J. de Geus, R. H. J. Peerlings, M. G. D. Geers, Microstructural topology effects on the onset of ductile failure in multi-phase material: A systematic computational approach, International Journal of Solids and Structures 67-68 (2015) 326–339. doi:10.1016/j.ijsolstr.2015.04.035.

[37] T. W. J. de Geus, F. Maresca, R. H. J. Peerlings, M. G. D. Geers, Microscopic plasticity and damage in two-phase steels: On the competing role of crystallography and phase contrast, Mechanics of Materials 101 (2016) 147–159. doi:10.1016/j.mechmat.2016.07.014.

[38] S. K. Yerra, G. Martin, M. Véron, Y. Bréchet, J. D. Mithieux, L. Delannay, T. Pardoen, Ductile fracture initiated by interface nucleation in two-phase elastoplastic systems, Engineering Fracture Mechanics 102 (2013) 77–100. doi:10.1016/j.engfracmech.2013.02.028.

[39] J. O. Andersson, T. Helander, L. Höglund, P. Shi, Thermo-Calc & DICTRA, computational tools for materials science, Calphad 26 (2002) 273–312.

[40] C. G. de Andrés, J. A. Jiménez, L. F. Alvarez, Splitting phenomena occurring in the martensitic transformation of Cr13 and CrMoV14 stainless

steels in the absence of carbide precipitation, Metallurgical and Materials Transactions A 27 (1996) 1799. doi:10.1007/bf02651929.

[41] A. Bénéteau, P. Weisbecker, G. Geandier, E. Aeby-Gautier, B. Appolaire, Austenitization and precipitate dissolution in high nitrogen steels: an in situ high temperature X-ray synchrotron diffraction analysis using the Rietveld method, Materials Science & Engineering A 393 (2005) 63. doi:10.1016/j.msea.2004.09.054.

[42] G. F. Vander Voort, Metallography, Principles and Practice, ASM International, 1984.

[43] M. D. Abramoff, MagalhaesP.J., RamS.J., Image Processing with ImageJ, Biophotonics International 11 (2004) 36–42.

[44] D. Lassance, F. Scheyvaerts, T. Pardoen, Growth and coalescence of penny-shaped voids in metallic alloys, Engineering Fracture Mechanics 73 (2006) 1009–1034. doi:10.1016/j.engfracmech.2005.12.004.

[45] A. W. Hudgins, D. K. Matlock, The effects of property differences in multiphase sheet steels on local formability, Materials Science & Engineering A 654 (2016) 169–176. doi:10.1016/j.msea.2015.12.035.

[46] M. D. Taylor, K. S. Choi, X. Sun, D. K. Matlock, C. E. Packard, L. Xu, F. Barlat, Correlations between nanoindentation hardness and macroscopic mechanical properties in DP980 steels, Materials Science and Engineering a-Structural Materials Properties Microstructure and Processing 597 (2014) 431–439. doi:10.1016/j.msea.2013.12.084.

[47] Q. Furnémont, M. Kempf, P. J. Jacques, M. Göken, On the measurement of the nanohardness of the constitutive phases of TRIP-assisted multiphase steels, Materials Science & Engineering A 328 (2002) 26–32. doi:10.1016/S0921-5093(01)01689-6.

[48] W. C. Oliver, G. M. Pharr, Measurement of hardness and elastic modulus by instrumented indentation: Advances in understanding and refinements

to methodology, Journal of Materials Research 19 (2004) 3. doi:10.1557/jmr.2004.0002.

[49] S. Allain, O. Bouaziz, M. Takahashi, Toward a new interpretation of the mechanical behaviour of as-quenched low alloyed martensitic steels, ISIJ international 52 (2012) 717–722.

[50] G. Badinier, C. W. Sinclair, X. Sauvage, X. Wang, V. Bylik, M. Gouné, F. Danoix, Microstructural heterogeneity and its relationship to the strength of martensite, Materials Science & Engineering A 638 (2015) 329–339. doi:10.1016/j.msea.2015.04.088.

[51] J. R. Rice, D. M. Tracey, On the ductile enlargement of voids in triaxial stress fields, Journal of the Mechanics and Physics of Solids 17 (1969) 201. doi:10.1016/0022-5096(69)90033-7.

[52] B. I. Edelson, W. M. J. Baldwin, The effect of second phases on the mechanical properties of alloys, Trans. Quart. ASM 55 (1962) 230–250.

[53] F. Hannard, T. Pardoen, E. Maire, C. Le Bourlot, R. Mokso, A. Simar, Characterization and micromechanical modelling of microstructural heterogeneity effects on ductile fracture of 6xxx aluminium alloys, Acta Materialia 103 (2016) 558–572. doi:10.1016/j.actamat.2015.10.008.

[54] Y. Funakawa, T. Ujiro, Change in Yield Strength of Ultra Low Carbon Steels with Cr Addition, Tetsu-to-Hagane 96 (2010) 162–171. doi:10.2355/tetsutohagane.96.162.

[55] G. Avramovic-Cingara, Y. Ososkov, M. K. Jain, D. S. Wilkinson, Effect of martensite distribution on damage behaviour in DP600 dual phase steels, Materials Science & Engineering A 516 (2009) 7–16. doi:10.1016/j.msea.2009.03.055.

[56] Y. Ososkov, D. S. Wilkinson, M. Jain, T. Simpson, In-situ measurement of local strain partitioning in a commercial dual-phase steel, International Journal of Materials Research 98 (2007) 664. doi:10.3139/146.101526.

[57] M. C. Jo, J. Park, S. S. Sohn, S. Kim, J. Oh, S. Lee, Effects of untransformed ferrite on Charpy impact toughness in 1.8-GPa-grade hot-press-forming steel sheets, Materials Science & Engineering A 707 (2017) 65–72. doi:10.1016/j.msea.2017.09.027.

[58] A. M. Bettanini, L. Delannay, P. J. Jacques, T. Pardoen, G. Badinier, J.-D. Mithieux, Influence of microscopic strain heterogeneity on the formability of martensitic stainless steel, AIP Conference Proceedings 1896. doi:10.1063/1.5007967.

[59] G. Martin, S. K. Yerra, Y. Bréchet, M. Véron, J.-D. Mithieux, B. Chéhab, L. Delannay, T. Pardoen, A macro- and micromechanics investigation of hot cracking in duplex steels, Acta Materialia 60 (2012) 4646. doi:10.1016/j.actamat.2012.03.040.

[60] G. Martin, D. Caldemaison, M. Bornert, C. Pinna, Y. Bréchet, M. Véron, J. D. Mithieux, T. Pardoen, Characterization of the High Temperature Strain Partitioning in Duplex Steels, Exp Mech 53 (2012) 205–215. doi:10.1007/s11340-012-9628-y.